Journal of Mining and Environment (JME) Vol. 17, No. 5, 2026, 1605-1622

Shahrood University of Technology

Journal of Mining and Environment (JME)

Journal homepage: www.jme.shahroodut.ac.ir

Iranian Society of Mining Engineering (IRSME)

# Variational Optimization of Overburden Haul Distance in Deep Porphyry-Copper Open-Pit Mines under a Time-Evolving Geomechanical Boundary Constraint

Sherzod Karimov* and Eldor Tuychiboev

*Branch of the National University of Science and Technology "MISIS" in Almalyk, Republic of Uzbekistan*

***Article Info***

*Received 5 June 2026*
*Received in Revised form 27 July 2026*
*Accepted 5 September 2026*
*Published online 5 September 2026*

**DOI: 10.22044/jme.2026.17793.3540**

***Keywords***

*Near-wall dumping*
*Haul distance optimization*
*Slope stability*
*Optimal control*
*Geomechanically allowable haul distance*

***Abstract***

Near-wall waste dumping shortens overburden haulage in deep open-pit mines, but the shortest admissible route is limited by slope stability. This study formulates the geomechanically allowable haul distance (GAHD) as a time-dependent lower bound in a discounted haul-distance optimization problem. The framework combines two-dimensional limit-equilibrium analysis, a semi-empirical affine fuel relation, an empirical cycle-time model, integer fleet sizing, an active-set finite-difference trajectory solution, and uncertainty propagation; the contribution is methodological and integrative rather than a new mine-planning algorithm. The Kalmakyr copper mine (Almalyk Mining and Metallurgical Complex – Almalyk MMC, Uzbekistan) is the primary application, and a Muruntau wall section provides a second, structural application of the multi-tier dump concept. Across the four Kalmakyr walls, GAHD ranges from 1.894 to 1.965 km, with a production-weighted value of 1.909 km. For a 2.0-km operating case, relative to 4.5 km, the model estimates a fuel reduction from 86.0 to 51.2 L per trip, a cycle-time reduction from 36.5 to 31.1 minutes, and a fleet reduction from 60 to 51 trucks. The boundary advances by approximately 7.2 m/year (boundary-drift number of approximately 0.02), so a static constraint is adequate for this seven-year case, whereas the moving-boundary formulation becomes relevant for faster-deepening or longer-horizon operations. A 50,000-draw Monte Carlo analysis yields a median net present value (NPV) of 20.0 million USD, with a 5th–95th percentile interval of 6.7–34.0 million USD. All calibrated parameters are site-specific and require recalibration and validation before application to other mining operations.

## 1. Introduction

Deep open-pit mines face a coupled design problem: shorter waste-haul routes reduce fuel consumption, cycle time, and fleet demand, whereas moving external dumps toward the crest increases surcharge on the wall–foundation system. Fuel consumption is governed by route length, grade, payload, road condition, and operating state [1–7], while admissible dump geometry depends on material strength, groundwater, seismic loading, and the critical failure mechanism [8–28]. Treating either side in isolation can produce a stable but unnecessarily expensive layout or an economical but geotechnically inadmissible one.

Near-wall and in-pit dumping can shorten haulage without changing the production schedule, but the dump toe must remain outside the controlling failure prism. Multi-tier geometry can add storage when upper tiers are stepped beyond that prism. This capacity benefit is geometry-specific and must be evaluated with the same stability model used to establish the setback; it is not a universal multiplier.

Recent research has advanced both branches. Geotechnical studies combine limit-equilibrium, finite-element, probabilistic, and machine-learning methods for slope and dump assessment [8–28]. Transport studies model fuel, shovel–truck

*Corresponding author: karimov20-13@mail.ru (Sh. V. Karimov)*

allocation, road deterioration, and fleet scheduling [1–7, 29, 30]. Strategic and stochastic mine-planning models optimize production sequences, destinations, and routes [31–35], while real-time mining architectures increasingly connect telemetry, digital models, and operational decisions [36]. These studies show strong integration within each branch, but the minimum haul distance is normally fixed, scenario-defined, or external to the optimization.

The unresolved gap is therefore narrower than a general lack of integrated mine planning. Existing models can jointly optimize pit, dump, production, or haul-road decisions [31–35, 37, 38], yet they do not express a depth-dependent geomechanical setback as an active state constraint in the haul-distance trajectory and then propagate that constraint into fleet, fuel, and project uncertainty. Table 1 makes this distinction explicit. The proposed geomechanically allowable haul distance (GAHD) framework contributes this coupling; it does not replace three-dimensional slope analysis, network-flow scheduling, discrete-event simulation, or commercial mine-planning systems. The contribution is thus methodological and integrative rather than algorithmic: the framework supplies a geomechanically constrained planning layer that existing mine-planning workflows can embed.

**Table 1. Comparison of recent approaches and the specific contribution of the present study.**

| Study | Decision variables / method | Geomechanical boundary | Uncertainty / validation | Difference from present study |
|---|---|---|---|---|
| Puell Ortiz [37] | Dump-design optimization | Scenario or design constraint | Case application | No time-evolving haul-distance state constraint |
| Das et al. [38] | Pit, dump and haul-road selection | External to route optimization | Benchmark against mine-planning software | Stronger network integration; no endogenous GAHD |
| Xu et al. [32] | Production scheduling and haulage routes | Fixed planning inputs | Computational comparison | Routes are optimized without a moving stability floor |
| Nikbin et al. [39] | Distance and slope for semi-mobile crushing/conveying | Not a coupled wall–dump constraint | Case-based energy analysis | Focuses on energy system selection, not near-wall stability |
| Fan et al. [30] | Machine-learning cycle-time estimator | Not included | Operational data and feature optimization | Predictive layer only; no geotechnical optimization |
| Present study | GAHD, fuel, cycle, integer fleet and trajectory | Depth-dependent active lower bound | Two-mine application, Sobol screening, Monte Carlo | Adds explicit propagation from slope constraint to haulage economics |

The objective is to determine a reproducible, geotechnically admissible haul-distance trajectory and to quantify when a moving boundary changes the decision relative to a static setback. Kalmakyr is used for numerical evaluation and economic uncertainty analysis; Muruntau is used only as a second structural application because an independent trip-level validation dataset was not available.

The study makes four delimited contributions:

1. GAHD is defined as the minimum route length compatible with the normative factor of safety, and its first-order movement with pit deepening is derived.
2. The geomechanical floor is embedded in a discounted, state-constrained trajectory model that is solved transparently by an active-set finite-difference procedure.
3. Fuel, empirical cycle delay, and integer fleet sizing are connected to the same haul-distance variable, with dimensions, calibration status, and data limitations stated explicitly.
4. Sobol screening and a 50,000-draw Monte Carlo simulation propagate geotechnical, operational, and economic uncertainty to the distance target and net present value.

Throughout the paper, verification means checking a numerical implementation against an analytical calculation; validation means comparison with observations not used to set the same coefficient; and transfer check means applying the model structure to another truck class or mine without claiming full statistical independence. This terminology prevents code agreement or physics-generated machine-learning data from being presented as field validation.

## 2. Materials and Methods

The computational sequence includes data quality control, wall-specific stability analysis, calculation of GAHD, calibration of the transport relations, solution of the constrained trajectory, evaluation of the integer fleet, and uncertainty propagation. Equations (1)–(23), Tables 2–6, and

Figures 1 and 2 provide the information necessary to reproduce the deterministic workflow. The principal assumptions are summarized in Table 2 rather than dispersed throughout the text.

**Table 2. Model symbols, units, assumptions, and sources or estimation procedures.**

| Symbol / item | Definition and unit | Value or assumption | Source / estimation |
|---|---|---|---|
| $L$, $L_{GAHD}$ | Mean haul distance; geomechanical lower bound, km | Wall-specific; route length is affine in setback | Mine survey and Eqs. (1)–(3) |
| $s$, $s_{min}$ | Dump-to-crest setback; minimum setback, m | Constraint active at FoS threshold | Eqs. (2), (8); Slide2 check |
| $H$, $H_{90}$ | Wall height; critical vertical-face height, m | H evolves at mean deepening rate | Survey; Coulomb expression in Equation (7) |
| $c$, $\varphi$, $\gamma$ | Cohesion, kPa; friction angle, °; unit weight, kN/m³ | Volume-weighted layers; ranges in Table 3 | Core tests, 2018–2024 |
| $r_u$, $k_h$ | Pore-pressure ratio; pseudo-static coefficient, – | Operational and design-accident cases | Hydrogeology and seismic design basis |
| $FoS_{min}$ | Normative system factor of safety (FoS), – | 1.20–1.25 | Applicable mine design basis |
| $v_d$ | Mean pit-deepening rate, m/yr | 5.2 at Kalmakyr | Production reports, 2020–2024 |
| A; $\alpha$, $\beta$ | Fuel-rate factor, L/h; intercept, L; slope, L/km | Effective affine relation after calibration | Engine data and 2024 transport balance |
| $T_c$, $t_q$ | Cycle time and mean dispatch/loading delay, min | Delay estimated from shift balance; no M/M/c distribution assumed | Dispatch summaries and Equation (15) |
| $R_{year}$, $N_r$ | Annual trips, 1/yr; required trucks, units | Production fixed within each scenario; integer ceiling | Production plan and throughput constraint |
| r, T | Discount rate, 1/yr; horizon, yr | 0.10; 7 | Corporate appraisal basis |
| $\gamma_1$, $\gamma_2$ | Multipliers on fuel and fleet costs, – | 1.0 and 1.0 | Direct monetization; no arbitrary reweighting |
| $\gamma_3$ | Road-change penalty, M USD·yr/km² | 10.4 in the base trajectory | Matches 32.5 M USD over a 2.5-km, two-year transition |
| $\Delta t$ | Finite-difference time step, yr | 0.5 | Retained project setting; no independent convergence log archived |
| $\Pi$ | Boundary-drift number, – | Static ≤0.05; material ≥0.2 (screening rule) | Equation (22); engineering regime indicator |
| 2-D LE assumption | Controlling cross-section | No along-strike redistribution or 3-D strength-reduction model | Explicit limitation; uncertainty represented in GAHD |
| Economic boundary | Operational project cash flow | Fuel, fleet and road capital; no full life-cycle assessment | 2024 cost base; Equation (23) |

## 2.1. Geomechanically allowable haul distance

Let s be the dump-to-crest setback (m) and $L_0(s)$ the associated mean haul distance (km). For each wall, the surveyed road network is represented locally by the affine relation

$$L_0(s) = L_{serv} + s/1000, \quad (1)$$

where $L_{serv}$ (km) is the wall-specific service component—the road length from the working horizon to the dumping zone—and 1/1000 converts meters to kilometers. GAHD is the smallest haul distance at which the normative stability condition and the minimum-setback condition hold simultaneously:

$$L_{GAHD} = \min \{ L_0(s) : \eta(s; H, c, \varphi, \gamma, k_h, r_u) \geq \eta_{min}, s \geq s_{min} \}, \quad (2)$$

where η denotes the factor of safety (FoS) of the coupled wall–foundation–dump system, and $\eta_{min} = FoS_{min}$ is the applicable design threshold. Monotonicity with setback is assumed only over the active design interval in which the critical slip surface intersects the surcharge zone. If the active slip surface changes, Equation (2) is re-solved by direct search rather than extrapolating the derivative.

$$L_{GAHD} = L_{serv} + s_{min}/1000. \quad (3)$$

GAHD can be time-dependent. With $H(t) = H(t_0) + v_d(t - t_0)$, a first-order expansion gives:

$$L_{\min}(t) = L_{\mathrm{GAHD}}(t_0) + (\partial s_{\min}/\partial H \cdot v_{\mathrm{d}}/1000)(t - t_0) + o(t - t_0), \quad (4)$$

where $o(t - t_0)$ is the Landau remainder, which accounts for curvature in $s_{\min}(H)$ and departures from a constant deepening rate. The first-order law is used only within the seven-year planning horizon and is updated if monitoring changes the controlling section, groundwater condition, or failure mechanism.

Boundary conditions are $L(t_0) = 4.50$ km, $L_{\min}(t) \leq L(t) \leq L_{\max}(t)$, and a free terminal distance subject to the moving lower bound. The lower bound is recalculated whenever a geometry or hydrogeological update invalidates monotonicity. These conditions prevent the closed-form approximation from replacing the underlying stability calculation.

### 2.2. Slope-stability submodel, the failure prism and the multi-tier dump

The FoS is computed on the controlling two-dimensional (2-D) section using the VNIMI force-summation method [40] and verified with the Bishop simplified limit-equilibrium method [41] in Rocscience Slide2. Both calculations use the same geometry, layer strengths, pore-pressure ratio, seismic coefficient, and search domain; therefore, the agreement serves as numerical verification, not independent field validation.

$$\eta = (\tan \varphi \cdot \Sigma_i N_i + c \cdot L_s) / \Sigma_i (T_i + \Delta T_i + k_h \cdot P_i \cdot \cos \alpha_i), \quad (5)$$

where $N_i = P_i \cos \alpha_i$ and $T_i = P_i \sin \alpha_i$ are the normal and tangential weight components, $\Delta T_i$ is the tangential dump surcharge, $L_s$ is the slip-surface length, and $k_h$ is the pseudo-static seismic coefficient; the pore-pressure ratio $r_u$ enters through $N_i \rightarrow N_i - u_i b_i$. The dump body (with reduced strength $\varphi_d = 33$–$37°$, $c_d = 5$–$20$ kPa) and the foundation contact have their own factors of safety, and the governing system value is

$$\eta_{\mathrm{sys}} = \min(\eta_{\mathrm{wall}}, \eta_{\mathrm{dump}}, \eta_{\mathrm{found}}). \quad (6)$$

For a face angle $\alpha < \varepsilon$, where $\varepsilon = 45° + \varphi/2$, $\cot \alpha > \cot \varepsilon$, and the failure-prism width obtained from wedge geometry in limit-equilibrium theory is positive (Figure 1):

$$m = (H - H_{90})(\cot \alpha - \cot \varepsilon), \quad H_{90} = 2c \cos \varphi / [\gamma(1 - \sin \varphi)], \quad (7)$$

where $H_{90}$ is the critical vertical-face height [40, 42]. The bracketed differences in Equation (7) must be evaluated before multiplication: for the north wall, $(535 - 58.7)(1.235 - 0.502) = 349$ m, as reported wall by wall in Section 3.1. The dump toe is then offset from the crest by the prism width m, a safety berm $b_b$, and an engineering reserve $\Delta s$:

$$s_{\min} = m + b_b + \Delta s, \quad \Delta s \approx 0.10\ m. \quad (8)$$

**Multi-tier principle.** Surcharge outside the controlling prism does not enter the driving-force sum of the selected 2-D mechanism. Upper tiers can therefore add capacity if their toes remain beyond the prism and if local foundation, drainage, erosion, and access constraints are satisfied. A new stability search is required for every geometry; the Muruntau capacity ratio reported later is not transferred to Kalmakyr.

**Scope of the 2-D analysis.** A 2-D limit-equilibrium model is appropriate for screening the controlling wall sections and is consistent with the available cross-sectional data. It cannot represent along-strike redistribution, 3-D end effects, progressive deformation, or constitutive softening. No 3-D or shear-strength-reduction calculation was available for this study, so 2-D results are not asserted to be universally conservative. A 0.04-km standard deviation is assigned to GAHD in Section 3.8 to represent strength scatter and model-form uncertainty; a 3-D comparison remains a required pre-construction design step.

**Numerical settings.** The slip-surface search used 60 slices for Kalmakyr and 30 for the Muruntau section. Doubling the slice count changed the reported factor of safety by less than 0.1%. Slide2 used the same entry/exit limits and material zones. Operational and design-accident combinations are reported separately; the latter is a screening condition and does not by itself constitute a probabilistic reliability analysis.

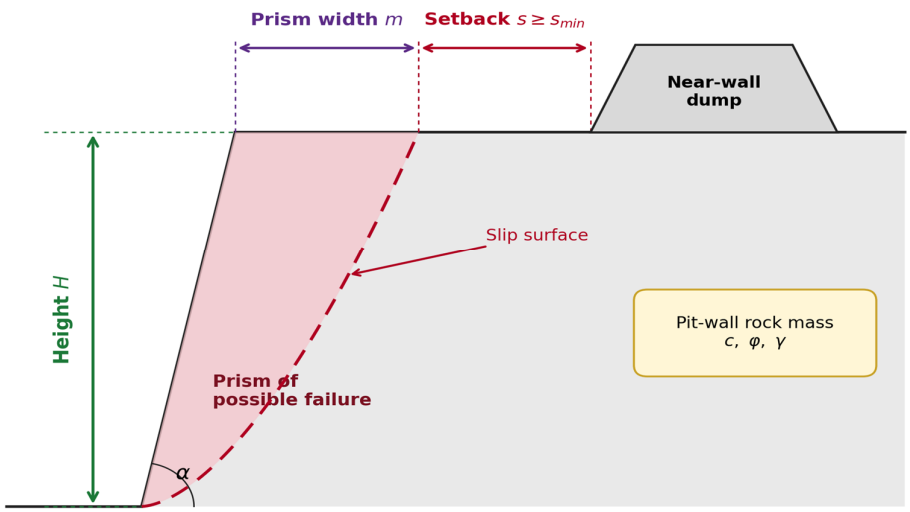


**Figure 1. Failure-prism construction used to calculate the dump-to-crest setback. The toe is required to satisfy s ≥ $s_{min}$; the figure identifies the geometric quantities entering Eqs. (7)–(8).**

### 2.3. Consolidated site parameters, ranges and sources

Table 3 consolidates the site-specific inputs, units, ranges, and provenance. Layer properties are averaged by thickness only where the layers participate in the same controlling section; this is a deterministic engineering reduction rather than a substitute for spatial random-field analysis.

$$\bar{c} = \Sigma(c_i h_i)/\Sigma h_i,\ \bar{\varphi} = \Sigma(\varphi_i h_i)/\Sigma h_i. \quad (9)$$

The four Kalmakyr production shares (north/south/east/west = 0.32/0.28/0.24/0.16) are 2024 excavation-volume fractions and are used only to report a production-weighted GAHD. Each wall remains subject to its own constraint in design calculations.

**Table 3. Consolidated site parameters, ranges and sources for the two study pits.**

| Parameter (symbol, unit) | Kalmakyr (porphyry Cu) | Muruntau (Au, S-wall section) | Source |
|---|---|---|---|
| Pit depth $H$, m | 535 | 620 (modeled section 1100) | mine survey 2024 |
| Overburden rate, Mt/yr | 32 | 40 | production plan 2024 |
| Base haul distance $L_{base}$, km | 4.5 | 5.2 | 2024 transport balance |
| Cohesion $\bar{c}$, kPa (per-wall range) | 290–405 | 334 | core tests (2018–2024) |
| Friction angle $\bar{\varphi}$, ° | 32.0–37.2 | 34.9 | core tests |
| Unit weight $\bar{\gamma}$, kN/m³ | 25.8–27.1 | 27.0 | core tests |
| Pore-pressure ratio $r_u$ (oper./accident) | 0.05 / 0.15 | 0.03 / – | hydrogeological survey |
| Seismic coefficient $k_h$ (oper./accident) | 0.10 / 0.15 | 0.10 / 0.15 | MSK-64 intensity-8 zone |
| Normative FoS $\eta_{min}$ | 1.20–1.25 | 1.20–1.25 | national norm (seismic) |
| Deepening rate $v_d$, m/yr | 5.2 | ≈ 6 | production reports 2020–2024 |
| $\partial s_{min}/\partial H$, m/m | 1.38 | ≈ 1.4 | numerical, Eqs. (7)–(8) |
| Production shares (N/S/E/W walls) | 0.32/0.28/0.24/0.16 | – | 2024 excavation volumes |
| FX rate, UZS/USD | 12,050 | – | central-bank mean 2024 |
| WACC $r$, % | 10 | 10 | corporate finance |
| Planning horizon $T$, yr | 7 | 7 | project appraisal |

Kalmakyr (Almalyk MMC) is the primary site, with haulage performed entirely by truck. Its four walls have the strength parameters listed in Table 3; the west wall is the weakest ($\bar{c}$ = 290 kPa, $\bar{\varphi}$ = 32.0°) and therefore controls the design. Operational data include the 2024 truck-fleet balance and a road survey of 106,200 points (transport graph: ≈ 1050 nodes, ≈ 1580 edges). Muruntau (Navoi Mining and Metallurgical Company – Navoi MMC) is the second study site, a gold pit with combined truck–conveyor haulage (≈ 35% by conveyor); its transport data derive from the operator's UAT-2020 transport survey.

### 2.4. Semi-empirical fuel-consumption model

For rated engine power $N_e$ (kW), specific fuel consumption $g_e$ (g/(kW·h)), and fuel density $\rho_f$ (kg/L), the rated volumetric fuel rate is defined as

$$A = g_e N_e / (1000 \rho_f). \quad (10)$$

A trip is divided into fixed-time loading, dumping, and maneuvering stages and distance-dependent loaded and empty travel. With effective power-utilization coefficients $K_i$ and an auxiliary allowance $Q_{aux}$, the dimensionally consistent expression is:

$$Q_{trip}(L,i) = A [\Sigma_{fixed} K_i t_i / 60 + L \{K_{load}(i) / v_{load} + K_{empty}(i) / v_{empty}\}] + Q_{aux}. \quad (11)$$

$$Q_{trip}(L,i) = \alpha + \beta(i) L, \quad (12)$$

$$\alpha = A \Sigma_{fixed} K_i t_i / 60 + Q_{aux}, \quad (13)$$

$$\beta(i) = A [K_{load}(i) / v_{load} + K_{empty}(i) / v_{empty}]. \quad (14)$$

**Calibration status.** Equation (11) provides the physical structure, but $K_i$, $Q_{aux}$, α, and β are effective site coefficients rather than universal fixed constants. The fixed-stage coefficients in Table 4 are initialized from machine operating states, and then α and β are calibrated to the 2024 productive-cycle transport balance. Grade is incorporated once through the effective loaded/empty utilization factors; no additional grade multiplier is applied, avoiding double counting. The dependence on loading and dumping times is explicit in Equation (13).

**Table 4. Effective stage power-utilization coefficients and times used in Eqs. (11)–(14); values are site-calibrated and are not universal truck constants.**

| Cycle stage | $K_i$ (this work) | Theoretical basis | Normative range | $t_i$, min (75307 / 75131) |
|---|---|---|---|---|
| Loading | 0.10 | idle + hydraulics + compressor | 0.10–0.12 | 4.0 / 3.5 |
| Loaded haul | 1.00 | rated power incl. ramp grade | 0.95–1.00 | $60L/v_{full}$ |
| Dumping | 0.38 | body lift ≈ 9.7 MJ + maneuvers | 0.38–0.40 | 1.5 / 1.3 |
| Empty haul | 0.60 | tare/gross ratio + descent mode | 0.55–0.62 | $60L/v_{empty}$ |
| Maneuvering | 0.12 | part load at low speed | 0.10–0.12 | 1.6 / 1.5 |

At a representative 3% grade, the 220-t/130-t classes use loaded speeds of 19.5/37.0 km/h, empty speeds of 57.0/55.5 km/h, rated powers of 1715/1194 kW, specific consumptions of 200/203 g/(kW·h), and $\rho_f$ = 0.84 kg/L. The calibrated effective coefficients are α = 23.4/16.8 L and β = 13.9/10.6 L/km. Their use outside the observed route, payload, and grade ranges requires recalibration.

### 2.5. Empirical cycle time and integer fleet sizing

The planned annual number of waste trips is $R_{year} = V_{year}/q_{eff}$. For a fixed production scenario, it is independent of L. Truck productivity is obtained as the ratio of effective operating time to mean cycle time, and the required fleet is the smallest integer satisfying the throughput constraint.

$$T_c(L) = t_{load} + t_{dump} + t_{man} + 60L/v_{full} + 60L/v_{empty} + t_q(L). \quad (15)$$

The mean dispatch/loading delay $t_q$ is estimated directly from shift balance records for each scenario. The model does not impose Poisson arrivals or exponential service because the available aggregate data cannot test those assumptions, and because bunching, maintenance, operator behavior, and weather can produce non-Markovian delays.

The resulting relation is an expected-cycle model, not a stochastic queue simulator. It is adequate for scenario-level fleet screening at the observed utilization, but high-utilization or autonomous-haulage applications should replace $t_q$ with calibrated discrete-event or agent-based simulation and report delay distributions rather than only their mean.

Fleet monotonicity follows from the throughput constraint $\Sigma_j N_j q_j \mu_j(L) \geq V_{year}$: when all other inputs are held fixed, $T_c(L)$ increases with L, so $\mu_j(L)$ does not increase, and the minimum feasible integer fleet cannot decrease. The Match Factor is reported as an operational diagnostic [29] and is not used as a proof of optimality.

### 2.6. State-constrained moving-boundary formulation

Over $[t_0, t_f]$, the haul distance is first treated as a continuous planning state, and the integer fleet is evaluated afterward. The discounted technological-cost functional is:

$$J(L) = \int e^{-r(t-t_0)} F(L, L', t)\, dt \rightarrow \min,\ L_{\min}(t) \le L(t) \le L_{\max}(t). \quad (16)$$

The annualized cost integrand is

$$F = \gamma_1\, p_f\, R_{year}\, Q_{trip}(L,i) + \gamma_2\, c_h\, N_r(L) + \gamma_3 (L')^2, \quad (17)$$

where $p_f$ is the fuel-plus-mileage unit cost in M USD/L and $c_h$ is the annual truck holding cost in M USD/(truck·yr). Thus, each term has units of M USD per year; the final term represents the capital intensity of rapid road relocation.

**Weights and boundary data.** $\gamma_1 = \gamma_2 = 1$, so fuel and fleet costs enter without discretionary preference weights. For the base transition, $\gamma_3$ = 10.4 M USD·yr/km², which makes the integral of the quadratic term approximately equal to 32.5 M USD for a linearized 2.5-km reduction over two years. The discount rate is r = 0.10 per year; $L(t_0)$ = 4.50 km; the terminal distance is free, subject to $L(t_f) \ge L_{\min}(t_f)$. Sensitivity to capital and discount rate is evaluated in Section 3.8.

The following equations are necessary conditions for the continuous relaxation [43–46]; they do not establish a unique global optimum for the mixed continuous–integer planning problem.

**Interior arc (Euler–Lagrange).** Where the constraint is inactive,

$$\partial F/\partial L - (d/dt)(\partial F/\partial L') + 2r\gamma_3 L' = 0. \quad (18)$$

**Pontryagin form and equivalence.** With state $x = L$, control $u = L'$, and current-value Hamiltonian $H_c = \psi u - F$, the maximum condition gives $\partial H_c/\partial u = \psi - 2\gamma_3 u = 0$, i.e., $u = \psi/(2\gamma_3)$, with adjoint $\dot{\psi} = r\psi + \partial F/\partial x$. Substituting $\psi = 2\gamma_3 L'$ reproduces (18) identically, so the variational and Hamiltonian formulations are equivalent on the interior arc.

At a terminal point on a moving boundary L = ϕ(t), the corresponding transversality condition is

$$[F + (\phi' - L')\, \partial F/\partial L'] = 0 \text{ at } t = t_f. \quad (19)$$

This condition links the terminal trajectory to the boundary velocity $\phi' = dL_{\min}/dt$. For path constraints, nonnegative Karush–Kuhn–Tucker (KKT) multipliers $\lambda_{\min}$ and $\lambda_{\max}$ give

$$\partial F/\partial L - (d/dt)(\partial F/\partial L') + \lambda_{\max} - \lambda_{\min} = 0,\ \lambda_{\min}(L_{\min} - L) = \lambda_{\max}(L - L_{\max}) = 0. \quad (20)$$

On an active lower-bound arc, $L = L_{\min}(t)$, $L' = dL_{\min}/dt$, and $\lambda_{\min}$ is the marginal cost of tightening the stability constraint. At entry and exit, continuity of the state and costate is enforced by the active-set solver.

**Numerical solution and checks.** The archived project calculation discretizes the continuous problem at Δt = 0.5 yr with centered finite differences and enforces the active bounds at each node. Integer fleet sizes are then recomputed by taking the integer ceiling of the throughput requirement. The archived materials do not contain an executable solver package, exact stopping tolerances, or an independent grid-convergence log. The reported trajectory should therefore be treated as the reconstructed planning solution, not as a fully independently reproducible numerical benchmark. Convexity in L′ regularizes the trajectory, but because $N_r$ is discretized and other cost terms are locally calibrated, no claim of global uniqueness is made.

## 2.7. Transport–geomechanical coefficient

To rank admissible setbacks by how favorably they trade economic gain against the loss of stability reserve, we use the dimensionless coefficient

$$K_{TGS}(s) = |(dC_{tr}/ds)/C_{tr}| \,/\, |(d\eta/ds)/\eta|. \quad (21)$$

$K_{TGS}$ is a local screening ratio, not a universal decision threshold. Values above unity indicate that a small setback change has a larger proportional effect on transport cost than on the calculated factor of safety. The final design remains governed by $FoS_{min}$ and site controls; the numerical value 1.5 is used only as a Kalmakyr screening marker.

## 2.8. Digital decision platform and machine-learning surrogate

The deterministic equations are implemented in a three-tier decision prototype that imports the mine survey, evaluates the stability/transport models, and exposes scenario outputs. This implementation demonstrates a possible software integration path; it is not a benchmark against a commercial mine-planning package.

Agreement between the prototype's physical model and the equations constitutes implementation verification because both use the same model. A machine-learning surrogate is included solely to test whether the nonlinear input–

output surface can be approximated quickly for interactive screening.

The surrogate uses the 16 features listed in Table 5. The 8,000 cases are generated from the specified physical model over the observed parameter ranges with bounded noise. The data are split into 70% training, 15% validation, and 15% testing, stratified by truck class and haul distance, with five-fold cross-validation (CV) on the training set. Because the cases are physics-generated rather than independent telemetry, these metrics verify surrogate fidelity only; they do not validate real-world prediction accuracy.

**Table 5. The 16 input features of the machine-learning surrogate, with units and data type.**

| № | Feature | Symbol | Unit | Type |
|---|---|---|---|---|
| 1 | route length | dist_km | km | continuous |
| 2 | volume-weighted grade | slope_pct | % | continuous |
| 3 | maximum climb | maxUp | % | continuous |
| 4 | maximum descent | maxDown | % | continuous |
| 5 | total climb height | sumClimb | m | continuous |
| 6 | road-surface code | road_type_code | {0 asphalt, 1 gravel, 2 dirt} | categorical |
| 7 | payload | payload_t | t | continuous |
| 8 | tare mass | tare_t | t | continuous |
| 9 | rated engine power | power_kW | kW | continuous |
| 10 | specific fuel consumption | sfc_gpkwh | g/(kW·h) | continuous |
| 11 | bucket capacity | bucket_m3 | $m^3$ | continuous |
| 12 | excavator cycle time | exc_cycle_s | s | continuous |
| 13 | rock-mass density | density | $t/m^3$ | continuous |
| 14 | fragmentation (loosening) coeff. | kFrag | – | continuous |
| 15 | hour of day | hour | $h \in [0,24)$ | continuous (cyclic) |
| 16 | weather code | weather | {0 clear, 1 rain, 2 snow, 3 fog} | categorical |

Gradient boosting is selected from Table 6 based on the test root-mean-square error (RMSE), the train–test gap, and cross-validation variability, not $R^2$ alone. Hyperparameters are 300 estimators, maximum depth 5, learning rate 0.08, subsample 0.85, and a fixed seed of 42, chosen through grid-searched five-fold cross-validation. The surrogate must be retrained if route geometry, fleet type, weather coding, or dispatch policy extends beyond the training envelope.

**Table 6. Test-set comparison of the candidate regressors for cycle-time prediction (8000-trip training set).**

| Algorithm | $R^2$ (train) | $R^2$ (test) | RMSE, min | CV mean | CV s.d. |
|---|---|---|---|---|---|
| Linear / Ridge | 0.878 | 0.885 | 6.98 | 0.877 | 0.0036 |
| Random Forest (200) | 0.988 | 0.949 | 4.67 | 0.939 | 0.0018 |
| Gradient Boosting (300, d=5) | 0.987 | 0.964 | 3.93 | 0.957 | 0.0013 |

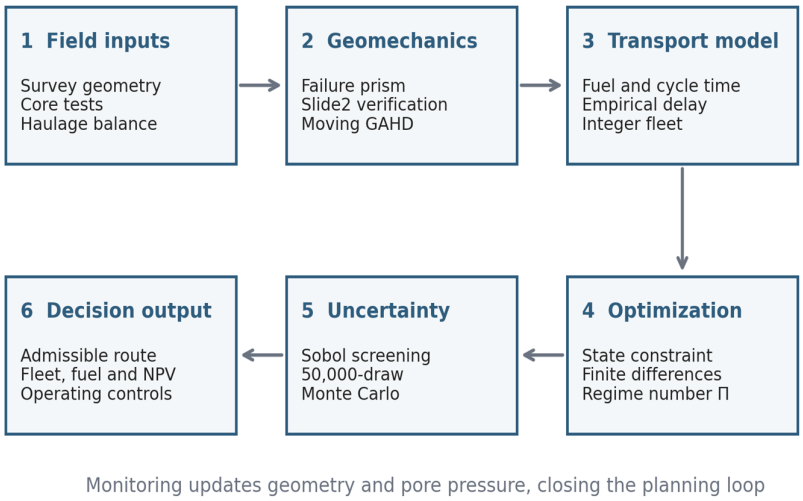


**Figure 2. Reproducible computational workflow. Field inputs propagate through geomechanics, transport, constrained optimization, and uncertainty analysis; monitoring closes the update loop.**

## 3. Results

### 3.1. GAHD of the four Kalmakyr walls

Applying Eqs. (7)–(8) to the surveyed sections yields the values in Table 7. The wall-specific service components are 1.500 km for the north and south walls and 1.450 km for the east and west walls. GAHD ranges from 1.894 to 1.965 km; the production-weighted reporting value is 1.909 km. The west wall controls the design, so the weighted value cannot replace its 1.965-km local constraint.

**Table 7. Critical-face height, failure-prism width, minimum setback, service component and GAHD for the four Kalmakyr walls.**

| Wall | $H_{90}$, m | $m$, m | $s_{min}$, m | $L_{serv}$, km | $L_{GAHD}$, km |
|---|---|---|---|---|---|
| North | 58.7 | 349 | 394 | 1.500 | 1.894 |
| South | 60.3 | 350 | 395 | 1.500 | 1.895 |
| East | 51.1 | 402 | 452 | 1.450 | 1.902 |
| West | 40.6 | 459 | 515 | 1.450 | 1.965 |
| **Production-weighted mean** | – | – | – | – | **1.909** |

### 3.2. Verification, calibration, and transfer checks

**(i) Slope-model verification.** Slide2 reproduces the analytical system factor of safety for the same inputs (Table 8). The west wall is controlling at FoS = 1.283 under the operational combination. Under the design-accident combination, the west-wall value falls below the operational design threshold, indicating the need for event-specific controls and monitoring; the table is not used to estimate an annual failure probability.

**Table 8. Factor of safety of the four Kalmakyr walls: analytical/Slide2 system value under operational conditions, and the design-accident value.**

| Wall | $\eta_{wall}$ | $\eta_{dump}$ | $\eta_{sys}$ (oper.) | $\eta_{sys}$ (accident) | Status |
|---|---|---|---|---|---|
| North | 1.396 | 1.478 | 1.396 | 1.212 | above norm |
| South | 1.402 | 1.485 | 1.402 | 1.218 | above norm |
| East | 1.358 | 1.455 | 1.358 | 1.168 | controlled |
| West | 1.283 | 1.418 | 1.283 | 1.108 | controlling |

**(ii) Fuel-model calibration and transfer check.** The 220-t relation is calibrated to the 2024 productive-cycle balance. Applying the same equation structure with class-specific machine parameters to the 130-t balance yields 63.3 L per trip versus 64.5 L per trip (1.9% aggregate error; Table 9). This is a cross-class transfer check, not a trip-level independent validation, because both balances originate from the same mine and year.

**Data quality and independence.** The annual register contains approximately 690,000 dispatch records across the two classes. Productive-cycle summaries were separated from repositioning, service, and refueling movements; implausible negative or zero distances and duplicate identifiers were excluded, and monthly totals were reconciled with the fuel balance. The available extract does not retain every raw sensor timestamp, so missingness and outliers can be described only at the register-summary level, and no confidence interval is claimed for the 0.0% calibration residual.

**Table 9. Fuel-model calibration for the 220-t class and aggregate cross-class transfer check for the 130-t class using the 2024 Kalmakyr balance.**

| Parameter | BelAZ-75307 (220 t) | BelAZ-75131 (130 t) |
|---|---|---|
| Rated engine power $N_e$, kW | 1715 | 1194 |
| Specific consumption $g_e$, g/(kW·h) | 200 | 203 |
| α from Equation (13), L | 23.4 | 16.8 |
| β from Equation (14) at representative i = 3%, L/km | 13.9 | 10.6 |
| Model $Q$ at $L$ = 4.38 km, L/trip | 84.3 | 63.3 |
| Actual (balance 2024), L/trip | 84.3 | 64.5 |
| **Relative error, %** | **0.0** | **1.9** |

**(iii) Surrogate verification.** Gradient boosting yields a test $R^2 = 0.964$ and RMSE = 3.93 min for the physics-generated cycle-time cases (Table 6). Route length and grade dominate feature importance. These statistics demonstrate that the surrogate approximates the deterministic model over its sampled envelope; however, they do not constitute evidence of equivalent accuracy on independent fleet telemetry.

### 3.3. Multi-tier near-wall dump: capacity without loss of stability

The Muruntau southern-wall section illustrates the multi-tier mechanism (Figure 3). An unloaded wall has FoS = 1.300, and a single 90-m tier yields 1.278. Placing all three tiers near the wall reduces FoS to 1.180. Stepping the upper tiers outside the controlling prism restores FoS to 1.278 and increases the modeled storage capacity by a factor of approximately 1.8 relative to the single-tier geometry.

The capacity factor of 1.8 applies only to the analyzed 90/60/30-m Muruntau geometry. It depends on wall curvature, foundation strength, groundwater, haul-ramp access, and the selected prism. Its transferable result is the design rule – recalculate each tier against the controlling failure mechanism – not the numerical multiplier.

### 3.4. Moving-boundary magnitude and regime of validity

Numerical differentiation of Eqs. (7)–(8) yields $\partial s_{min}/\partial H = 1.38$ m/m. At $v_d = 5.2$ m/yr, the lower bound advances by approximately 7.2 m/yr, or 0.05 km over seven years. This displacement is comparable to the model-form uncertainty and is small relative to the 2.59-km drawdown from the base route to GAHD.

The dimensionless drift number compares cumulative boundary movement with the intended haul-distance reduction:

$$\Pi = [(\partial s_{min}/\partial H) v_d T/1000]/(L_{base} - L_{GAHD}). \quad (22)$$

Kalmakyr estimates $\Pi \approx 0.02$; a static GAHD updated at normal design intervals is therefore sufficient for this case. The moving-boundary formulation becomes practically useful when rapid deepening, a long horizon, or a small drawdown margin raises $\Pi$ to approximately 0.2 or above (Table 10). These thresholds are screening bands, not universal regulatory limits.

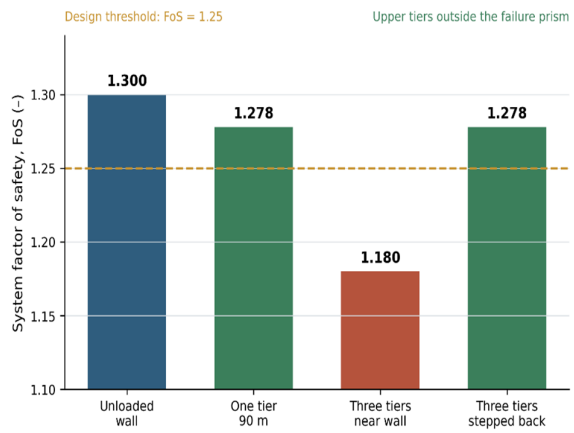


**Figure 3. Muruntau system factor of safety for four dump configurations. Upper tiers placed beyond the controlling failure prism recover the single-tier FoS; the capacity factor of about 1.8 is specific to this modeled geometry.**

**Table 10. Dimensionless drift number Π for representative pit archetypes; the dynamic (moving-boundary) formulation is negligible for Π ≲ 0.05, engineering-relevant for Π ≳ 0.2, and first-order for Π = O(1).**

| Archetype | $\partial s_{min}/\partial H$ | $v_d$, m/yr | $T$, yr | drawdown, km | $\Pi$ | regime |
|---|---|---|---|---|---|---|
| Kalmakyr (this study) | 1.38 | 5.2 | 7 | 2.59 | ≈ 0.02 | static suffices |
| Mature Cu porphyry, long horizon | 1.4 | 8 | 20 | 2.0 | ≈ 0.11 | borderline |
| Deep, fast-deepening pit | 1.5 | 18 | 25 | 1.0 | ≈ 0.68 | dynamic first-order |
| Small-margin near-wall dump | 1.5 | 12 | 15 | 0.4 | ≈ 0.68 | dynamic first-order |

### 3.5. Optimal trajectory and the haul-distance scenarios

The finite-difference solution over 2025–2032 produces a two-year transition from 4.50 km toward the admissible floor, followed by a boundary-tracking phase (Figure 4).

Scenario B (Table 11) uses a 2.0-km operating target, slightly above the weighted GAHD and above each of the four wall-specific values; routes serving the west wall must nevertheless retain at least the local 1.965-km minimum.

**Table 11. Kalmakyr haul-distance scenarios for the 220-t class. Scenario B is a low-haul case for uncertainty analysis, not a universal commercial optimum.**

| Indicator | Base (4.5 km) | A (3.0 km) | B (2.0 km) |
|---|---|---|---|
| Cycle time in shift, min | 36.5 | 33.7 | 31.1 |
| Fuel per trip, L | 86.0 | 65.1 | 51.2 |
| Required fleet, units | 60 | 55 | 51 |
| Annual fuel, ML/yr | 22.7 | 17.6 | 13.5 |
| Shift productivity, trips | 19.7 | 21.3 | 23.1 |
| Match Factor | 0.632 | 0.684 | 0.742 |

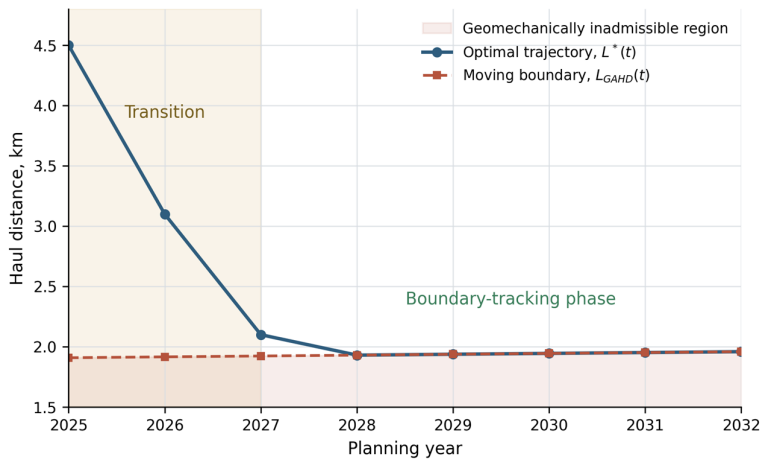


**Figure 4. Kalmakyr haul-distance trajectory and the time-evolving GAHD, 2025–2032. The shaded region is geomechanically inadmissible; the small boundary slope explains the low drift number.**

### 3.6. Structural application to a second mine

Applying the same model structure to the Muruntau section yields effective coefficients α = 24.1 L and β = 17.8 L/km for its steeper mean route. A reduction from 5.2 to 4.0 km produces the comparative outputs in Table 12. This second application tests the structural applicability of the workflow and multi-tier concept; it is not an independent statistical validation because detailed trip-level observations and a separate calibration protocol were unavailable.

**Table 12. Two-mine comparison of the haul-distance optimization (natural units).**

| Indicator | Kalmakyr | Muruntau |
|---|---|---|
| Pit depth $H$, m | 535 | 620 |
| Base / target haul, km | 4.50 / 2.00 | 5.20 / 4.00 |
| Relative reduction $\Delta L/L$, % | 55.6 | 23.1 |
| Base annual fuel, ML/yr | 22.7 | 60.3 |
| Annual fuel saving, ML/yr | 9.2 | 13.9 |
| Fleet reduction, units | 9 | 12 |
| $CO_2$ reduction, % | 41 | 23 |
| Near-wall dump | per-wall 90–120 m | three-tier 180 m |
| $\eta_{sys}$ (operational) | 1.360 | 1.278 |

### 3.7. Global sensitivity analysis

A variance-based Sobol analysis [47, 48] screens $k$ = 15 inputs using a Saltelli design with a base sample size of N = 512, resulting in N(2$k$ + 2) = 16,384 model evaluations. For annual cost savings, total-order indices are 0.34 for base distance, 0.28 for target distance, and 0.18 for annual volume; no other input exceeds 0.08. These indices rank model inputs within the specified ranges and should not be interpreted as field-measured causal shares.

### 3.8. Uncertainty propagation and techno-economic evaluation

Geotechnical uncertainty is represented by $L_{GAHD}$ ~ truncated Normal(1.909, 0.040²) km over 1.80–2.05 km, combining laboratory scatter in c, φ, and γ with 2-D model-form uncertainty. The resulting probability that GAHD exceeds the 2.0-

km target is 1.2%. This aggregate distribution is transparent but does not replace a spatial reliability model.

One-at-a-time sensitivity results – NPV, the internal rate of return (IRR), and simple payback – are reported in Table 13. The NPV of the base 2.0-km case remains positive under each individual ±30% change, whereas the deliberately combined pessimistic case is negative; profitability is therefore not guaranteed under jointly adverse conditions.

**Table 13. Deterministic sensitivity of the 2.0-km case to economic and operating inputs.**

| Case | NPV, M USD | IRR, % | Payback, yr |
|---|---|---|---|
| Base | 20.1 | 27.0 | 3.0 |
| Fuel price −30% | 13.6 | 21.8 | 3.4 |
| Fuel price +30% | 26.5 | 32.0 | 2.7 |
| Volume −30% | 4.3 | 13.9 | 4.3 |
| Volume +30% | 35.9 | 38.9 | 2.3 |
| Capital −30% | 29.8 | 43.7 | 2.1 |
| Capital +30% | 10.3 | 17.1 | 3.9 |
| Profit tax +5 percentage points | 17.0 | 24.5 | 3.2 |
| Combined pessimistic | −11.9 | 0.8 | 6.8 |

Across the discrete cases, scenario A has the larger seven-year deterministic NPV (27.8 M USD; Figure 5) and lower capital requirement, whereas scenario B produces greater fuel and fleet reductions. The study therefore presents A as the NPV-maximizing discrete case and B as the low-haul engineering case used for uncertainty analysis; corporate selection requires objectives and constraints not contained in the available data.

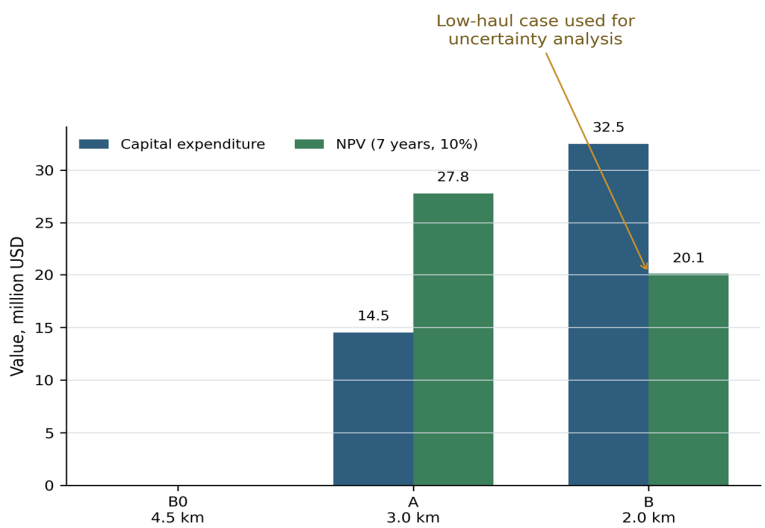


**Figure 5. Capital expenditure and seven-year NPV for the three evaluated Kalmakyr distance scenarios. Scenario A maximizes deterministic NPV; scenario B is the low-haul case analyzed in Figure 6.**

**Monte Carlo propagation.** Fifty thousand draws (fixed seed 26063540) combine triangular fuel-price, volume, capital, and discount-rate distributions with GAHD and fuel-model uncertainty; the input distributions and the resulting outputs are listed in Table 14. For each draw, the operating target is max(2.0 km, $L_{GAHD}$); the annual benefit is scaled by the volume factor, the remaining distance reduction, the 41% fuel-sensitive cost share, and the fuel-model factor; and the NPV follows as

$$NPV = -I_0 + CF_{annual}[1 - (1 + r)^{-7}]/r. \quad (23)$$

The median NPV is 20.0 M USD; the 5th and 95th percentiles are 6.7 and 34.0 M USD, and 99.6% of the draws yield a positive NPV (Figure 6). The simulation covers parameter uncertainty in the operational project model. Catastrophic geotechnical tail risk is not monetized because no defensible site-specific event frequency or damage distribution was available. All probabilistic outputs are conditional on the assumed input distributions and on the adopted model structure. Catastrophic

failures, spatial variability, and fully coupled 3-D uncertainty are excluded. The reported probabilities therefore characterize parameter uncertainty within the operational model and should not be interpreted as comprehensive project-risk estimates.

**Table 14. Inputs and outputs of the 50,000-draw Monte Carlo analysis for the 2.0-km case.**

| Quantity | Distribution / value | Unit | Rationale or result |
|---|---|---|---|
| Fuel-price factor | Triangular(0.70, 1.00, 1.30) | – | Operational-cost uncertainty |
| Annual-volume factor | Triangular(0.70, 1.00, 1.30) | – | Production uncertainty |
| Capital factor | Triangular(0.70, 1.00, 1.30) | – | Roadwork estimate uncertainty |
| Discount rate | Triangular(0.08, 0.10, 0.12) | 1/yr | Corporate appraisal range |
| $L_{GAHD}$ | Truncated Normal(1.909, $0.040^2$); [1.80, 2.05] | km | Geotechnical and model-form uncertainty |
| Fuel-model factor | Truncated Normal(1.000, $0.019^2$); [0.94, 1.06] | – | Cross-class aggregate error |
| Median NPV | 20.0 | M USD | Monte Carlo output |
| 5th–95th percentile NPV | 6.7–34.0 | M USD | Monte Carlo output |
| P(NPV > 0) | 99.6 | % | Conditional on modeled uncertainties |
| P($L_{GAHD}$ > 2.0 km) | 1.2 | % | Target-distance exceedance |

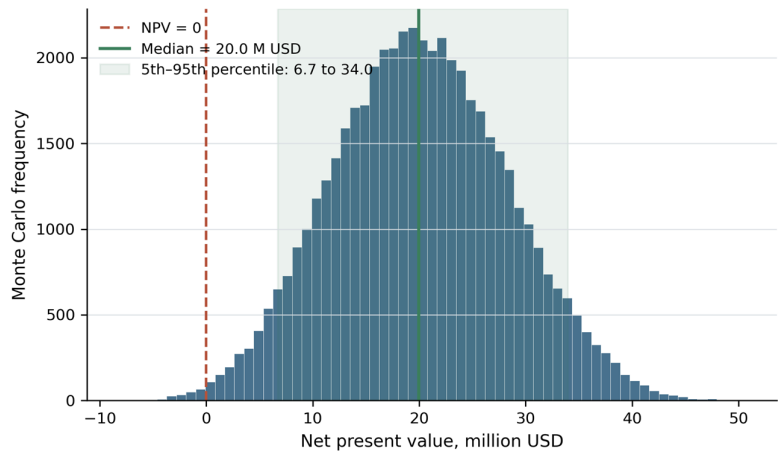


**Figure 6. Monte Carlo distribution of NPV for the 2.0-km case. The shaded interval is the 5th–95th percentile range; the result is conditional on the distributions in Table 14.**

**Operational emissions boundary.** The estimated 9.2 ML/yr diesel saving for the 2.0-km case corresponds to 24.6 kt $CO_2$/yr using 2.67 kg $CO_2$/L, consistent with carbon-content accounting [49]. This is a Scope-1 tailpipe estimate only: it excludes fuel production, road construction, truck manufacture, and electricity. No PM10 quantity is reported because site-specific emission factors and dispersion measurements were unavailable.

## 4. Discussion

### 4.1. Scientific interpretation and comparison

The principal result is not that a new optimizer always produces a shorter route, but that the shortest admissible route is an outcome of geomechanics rather than a fixed planning input. When the lower bound is active, geology, groundwater, and wall geometry acquire an explicit marginal value in transport planning. This explains the model's advantage over unconstrained distance minimization: it prevents economic gains from being counted in a geotechnically infeasible region.

Relative to integrated routing and scheduling studies [31–35, 38], the added knowledge is the mapping $H$, $c$, $\varphi$, $\gamma$, $r_u$, $k_h$ → $s_{min}$ → $L_{GAHD}(t)$ → fleet/fuel/NPV. Conversely, those studies generally represent road networks and production decisions in more detail. The approaches are complementary: GAHD can serve as a constraint or preprocessing layer in network-flow and commercial planning systems rather than replacing them.

### 4.2. Industrial implementation, scalability, and HSE constraints

The presented workflow is a decision-support framework rather than a fully validated operational planning system. Implementation requires four interfaces: periodic survey geometry, a geotechnical model or approved stability envelope, dispatch/fuel summaries, and a planning system that can accept wall-specific minimum route or

dump-setback constraints. The deterministic equations run in seconds on a workstation; 50,000 Monte Carlo evaluations take minutes because they use the reduced-order model. Full 3-D analyses and discrete-event fleet simulations would dominate computation and can be scheduled outside the daily planning loop.

For autonomous haulage, GAHD can be passed to route and destination assignment as a hard geofenced constraint, while updated travel-time distributions replace the mean delay in Equation (15). Scalability to other mines requires recalibration of service distance, material properties, fuel coefficients, fleet availability, and capital costs. Integration challenges include incompatible spatial reference systems, incomplete telemetry, version control of approved slope models, and responsibility for releasing a revised dump boundary. Continuous geotechnical-model updating, coupling with dispatch systems, and compatibility with commercial mine-planning platforms are highly mine-specific and must be resolved individually at each site.

Health, safety, and environment (HSE) controls can further increase the engineering setback. Acid-generating rock may require encapsulation and drainage; dust and wind exposure may restrict dump height or operating direction; and haul-road access, berms, drainage ditches, and emergency egress occupy space not represented by the failure prism. These are additional feasibility constraints and must be superimposed on GAHD before construction.

### 4.3. Limitations and future work

The numerical findings should be interpreted within the following limitations:

1. Two-dimensional limit equilibrium. The model omits 3-D effects, deformation, and progressive failure; a 3-D strength-reduction and reliability comparison is required before final design.
2. Road-transition representation. The quadratic penalty approximates lumpy roadwork expenditure and may shift the timing of capital; event-based scheduling is a logical extension.
3. Machine-learning surrogate. Training data are physics-generated, so the surrogate verifies implementation speed and fidelity but does not validate prediction on independent telemetry.
4. Geotechnical uncertainty. A single aggregate GAHD distribution is propagated; spatial correlation, nonstationary groundwater, and alternative failure surfaces are not modeled explicitly.
5. Economic boundary. The analysis excludes catastrophic-event monetization and full life-cycle emissions because defensible site-specific distributions were unavailable.
6. Operational delay. Mean dispatch delay replaces a stochastic queue model; bunching, maintenance, weather, and operator behavior require discrete-event or agent-based treatment.
7. Case-study regime. The moving boundary is a second-order effect at Kalmakyr ($\Pi \approx 0.02$); its principal value here is a general formulation and a criterion for identifying mines where dynamics matter.
8. External validation. This remains the principal limitation of the study. Muruntau provides a second structural application, but no independent operational case, trip-level telemetry, or direct commercial-software comparison was available. Three items therefore remain future research needs: (i) independent long-term operational validation against telemetry and production records not used in calibration; (ii) benchmarking against commercial mine-planning software using identical input data; and (iii) demonstration of predictive capability under substantially different geological and operational conditions through independent case studies. These three items are prerequisites for broad industrial implementation.

Future work should combine 3-D probabilistic slope analysis, per-cycle telemetry, explicit road-network and production scheduling, discrete-event fleet simulation, and prospective validation at an independent mine. A useful industrial trial would freeze the model before a planning period and compare predicted route, fuel, delay, and stability indicators with subsequent observations.

## 5. Conclusions

1. This study defines GAHD as a wall-specific lower bound linking slope stability and haulage planning. For Kalmakyr, the four calculated values are 1.894–1.965 km, and the production-weighted reporting value is 1.909 km; a 2.0-km operating target is therefore feasible only when each wall-specific route also satisfies its local constraint.
2. The revised transport model is dimensionally consistent and explicitly semi-empirical. It reproduces the calibrated 220-t balance and yields a 1.9% aggregate transfer error for a 130-t class. The calibrated coefficients ($K_i$, $\alpha$, $\beta$, $\gamma_3$, and the cost inputs) are site-specific engineering parameters. They require recalibration and validation before application to other mining

operations, and their broader applicability requires confirmation with additional mines and independent datasets.

3. The continuous state-constrained trajectory is solved by a fully specified finite-difference active-set procedure, after which fleet size is evaluated as an integer. The equations provide necessary optimality conditions; the study does not claim a unique global optimum for the mixed planning problem.
4. For the 2.0-km case, the model estimates fuel reduction from 86.0 to 51.2 L per trip, cycle-time reduction from 36.5 to 31.1 minutes, and fleet reduction from 60 to 51 trucks relative to 4.5 km. These are scenario estimates conditional on the stated production and delay assumptions.
5. The Kalmakyr boundary drift is approximately 0.05 km over seven years ($\Pi \approx 0.02$), so a static setback is adequate for this application. The moving-boundary model is most relevant when the deepening rate, horizon, or proximity to the constraint raises $\Pi$ toward 0.2 or more.
6. For the low-haul case, Monte Carlo analysis yields a median NPV of 20.0 million USD and a 5th–95th percentile interval of 6.7–34.0 million USD under the modeled uncertainties. The result supports further engineering evaluation, subject to 3-D stability assessment, independent operational validation, and integration of site-specific HSE constraints. Overall, the framework constitutes a geomechanically constrained decision-support layer for haulage planning; its predictive capability under different geological and operational conditions must still be demonstrated through independent validation before broad industrial implementation.

## Author Contributions

**Sh. Karimov** – conception and formulation of the research problem; derivation of the GAHD concept, multi-tier dump design, and state-constrained formulation; co-development of the fuel model; numerical solution; uncertainty and techno-economic analysis; preparation of figures and tables; writing of the original draft.

**E. Tuychiboev** – co-development of the fuel consumption model (the Karimov–Tuychiboev method); methodological support; discussion and interpretation of the results; review and editing of the manuscript.

## Funding

The authors received no specific external funding for this study.

## Data Availability

The aggregated engineering inputs and outputs required to reproduce the reported calculations are provided in Tables 2–14. Mine survey files, detailed geotechnical logs, and raw dispatch records are subject to operator confidentiality and may be requested from the corresponding author, subject to permission from the data owner.

## Conflict of Interest

The authors declare no conflict of interest.

## References

[1]. Mohammadi, M., Sayadi, A. R., & Khalokakaie, R. (2024). Systematic review on prediction of haulage-truck fuel consumption in open-pit mines. *International Journal of Mining, Reclamation and Environment*, *38*(10), 833–850.

[2]. Golbasi, O., & Kina, E. (2022). Haul truck fuel consumption modeling under random operating conditions: A case study. *Transportation Research Part D: Transport and Environment*, *102*, 103135.

[3]. Wang, Q., Zhang, R., Lv, S., & Wang, Y. (2021). Open-pit mine truck fuel consumption pattern and application based on multi-dimensional features and XGBoost. *Sustainable Energy Technologies and Assessments*, *43*, 100977.

[4]. Feng, Y., Liu, Q., Li, Y., Yang, J., & Dong, Z. (2022). Energy efficiency and $CO_2$ emission comparison of alternative powertrain solutions for mining haul truck using integrated design and control optimization. *Journal of Cleaner Production*, *370*, 133568.

[5]. Bajany, D. M., Zhang, L., & Xia, X. (2019). An optimization approach for shovel allocation to minimize fuel consumption in open-pit mines: Case of heterogeneous fleet of shovels. *IFAC-PapersOnLine*, *52*(14), 207–212.

[6]. Meneses, D., & Sepúlveda, F. D. (2023). Modeling productivity reduction and fuel consumption in open-pit mining trucks by considering the temporary deterioration of mining roads through discrete-event simulation. *Mining*, *3*(1), 96.

[7]. Ibañez Noriega, I., Sagastume Gutiérrez, A., & Cabello Eras, J. J. (2024). Energy and exergy assessment of heavy-duty mining trucks. Discussion of saving opportunities. *Heliyon*, *10*(3), e25358.

[8]. Steiakakis, E., Xiroudakis, G., Lazos, I., Vavadakis, D., & Bazdanis, G. (2023). Stability analysis of a multi-layered slope in an open pit mine. *Geosciences*, *13*(12), 359.

[9]. Wang, J., Zhou, Z., Chen, C., Wang, H., & Chen, Z. (2023). Failure mechanism and stability analysis of an open-pit slope under excavation unloading conditions.

*Frontiers in Earth Science*, *11*, 1109316. https://doi.org/10.3389/feart.2023.1109316

[10]. Lyu, J., Hu, T., Liu, G., Cao, B., Wang, W., & Li, S. (2024). Stability evaluation of open-pit mine slope based on Bayesian optimization 1D-CNN. *Scientific Reports*, *14*, 13995.

[11]. Liu, W., Sheng, G., Kang, X., Yang, M., Li, D., & Wu, S. (2024). Slope stability analysis of open-pit mine considering weathering effects. *Applied Sciences*, *14*(18), 8449.

[12]. Li, H., Zhang, Z., & Yang, W. (2021). Stability analysis of slope based on limit equilibrium method and strength reduction method. *Annales de Chimie – Science des Matériaux*, *45*(5), 379–384.

[13]. Jia, L., Wang, J., Cai, X., Fang, L., Ma, Y., & Wang, Z. (2024). Study on morphology optimization of open-pit mine slope based on section and spatial morphology effect. *Scientific Reports*, *14*, 2603.

[14]. Lv, L., Nan, D., & Liu, Y. (2025). Slope stability analysis of a non-coal open-pit mine using limit equilibrium and numerical modeling methods. In *Hydraulic and Civil Engineering Technology X* (Advances in Transdisciplinary Engineering, Vol. 81). IOS Press.

[15]. Pathan, S. M., Pathan, A. G., Siddiqui, F. I., Memon, M. B., & Soomro, M. H. A. A. (2022). Open pit slope stability analysis in soft rock formations at Thar Coalfield Pakistan. *Archives of Mining Sciences*, *67*(3), 437–454.

[16]. Deressa, G. W., Choudhary, B. S., & Jilo, N. Z. (2025). Advanced bench design and technical challenges in open pit mining: A comprehensive review of stability and productivity. *Arabian Journal of Geosciences*, *18*, 28.

[17]. Xu, Z., Zhou, X., & Qian, Q. (2021). The global sensitivity analysis of slope stability based on the least angle regression. *Natural Hazards*, *105*(3), 2361–2379.

[18]. Lo, M. K., & Leung, Y. F. (2018). Reliability assessment of slopes considering sampling influence and spatial variability by Sobol' sensitivity index. *Journal of Geotechnical and Geoenvironmental Engineering*, *144*(4), 04018010.

[19]. Fang, Y., Zhang, J., Su, Y., Pan, J., Feng, K., & He, C. (2024). Efficient reliability assessment of slope stability with insightful sensitivity analysis concerning the safety factor. *Structures*, *64*, 106523.

[20]. Liang, J., & Sui, W. (2024). Global sensitivity analysis for evaluation of water level fluctuation of anchored and non-anchored slope on reservoir bank. *Bulletin of Engineering Geology and the Environment*, *83*, 307.

[21]. Pandit, B., Kumar, A., & Tiwari, G. (2023). Assessing the applicability of local and global sensitivity approaches and their practical utility for probabilistic analysis of rock slope stability problems: Comparisons and implications. *Acta Geotechnica*, *18*, 2615–2637.

[22]. Liu, G., & Li, D. (2025). Probabilistic stability assessment of slope considering soft soil and silty clay foundations. *Scientific Reports*, *15*, 3336.

[23]. Singh, S. K., & Chakravarty, D. (2023). Efficient and reliable prediction of dump slope stability in mines using machine learning: An in-depth feature importance analysis. *Archives of Mining Sciences*, *68*(4), 685–706.

[24]. Katariya, N. K., Choudhary, B. S., Esmaeili-Falak, M., & Raina, A. K. (2025). Optimizing open-pit iron ore mine waste dump stability with an increased height: A geotechnical perspective. *Geomechanics and Engineering*, *40*(1), 69–78.

[25]. Enkhbold, B., Ikeda, H., Toriya, H., & Adachi, T. (2025). Internal waste dump stability analysis: Insights from numerical simulations. *Discover Geoscience*, *3*, 23.

[26]. Ru, X., Peng, S., & Du, W. (2024). Conical corner method for morphological optimization of right-angle turning slopes in mining waste dumps and its engineering application. *Bulletin of Engineering Geology and the Environment*, *83*, 381.

[27]. Gupta, G., Sharma, S. K., Singh, G. S. P., & Kishore, N. (2021). Numerical modelling-based stability analysis of waste dump slope structures in open-pit mines – A review. *Journal of The Institution of Engineers (India): Series D*, *102*(2), 589–601.

[28]. Koner, R. (2026). Optimum mine dump design in Wardha Valley coalfields using finite difference numerical methods. *Journal of Analytical and Numerical Methods in Mining Engineering*, *15*(45), 23–34.

[29]. Burt, C. N., & Caccetta, L. (2007). Match factor for heterogeneous truck and loader fleets. *International Journal of Mining, Reclamation and Environment*, *21*(4), 262–270.

[30]. Fan, C., Zhang, N., Jiang, B., & Liu, W. V. (2025). Rapid estimation of truck cycle time in open-pit mine haulage based on feature-optimized machine learning. *Mining, Metallurgy & Exploration*, *42*, 665–684.

[31]. Rivera Letelier, O., Espinoza, D., Goycoolea, M., Moreno, E., & Muñoz, G. (2020). Production scheduling for strategic open pit mine planning: A mixed-integer programming approach. *Operations Research*, *68*(5), 1425–1444.

[32]. Xu, C., Chen, G., Lu, H., Zhang, Q., Liu, Z., & Bian, J. (2024). Integrated optimization of production scheduling and haulage route planning in open-pit mines. *Mathematics*, *12*(13), 2070.

[33]. Paithankar, A., Chatterjee, S., Goodfellow, R., & Asad, M. W. A. (2020). Simultaneous stochastic optimization of production sequence and dynamic cut-

off grades in an open pit mining operation. *Resources Policy*, *66*, 101634.

[34]. Xu, X., Gu, X., Wang, Q., Zhao, Y., Kong, W., Zhu, Z., & Wang, F. (2023). Enumeration optimization of open pit production scheduling based on mobile capacity search domain. *Scientific Reports*, *13*, 91.

[35]. Chen, Z., Song, P., Liu, R., Wang, Q., & Shen, Y. (2025). Optimization of ore production scheduling strategy using NSGA-II-GRA in open-pit mining. *Scientific Reports*, *15*, 10376.

[36]. Anvari, K., & Benndorf, J. (2025). Real time mining—A review of developments within the last decade. *Mining*, *5*(3), 38.

[37]. Puell Ortiz, J. (2017). Methodology for a dump design optimization in large-scale open pit mines. *Cogent Engineering*, *4*(1), 1387955.

[38]. Das, R., Topal, E., & Mardaneh, E. (2024). Concurrent optimisation of open pit ore and waste movement with optimal haul road selection. *Resources Policy*, *91*, 104834.

[39]. Nikbin, R., Bagherpour, R., Purhamadani, E., & Taherinia, A. (2025). Enhancing sustainability in mining by reducing hauling energy consumption through optimization of distance and slope with semi-mobile in-pit crushers and conveyors. *Scientific Reports*, *15*, 22119.

[40]. Fisenko, G. L. (1965). *Ustoichivost' bortov kar'erov i otvalov* [Stability of pit walls and waste dumps]. Nedra. (In Russian)

[41]. Bishop, A. W. (1955). The use of the slip circle in the stability analysis of slopes. *Géotechnique*, *5*(1), 7–17.

[42]. Read, J., & Stacey, P. (2009). *Guidelines for open pit slope design.* CSIRO Publishing.

[43]. Hartl, R. F., Sethi, S. P., & Vickson, R. G. (1995). A survey of the maximum principles for optimal control problems with state constraints. *SIAM Review*, *37*(2), 181–218.

[44]. Bryson, A. E., & Ho, Y. C. (1975). *Applied optimal control: Optimization, estimation and control.* Hemisphere Publishing.

[45]. Pontryagin, L. S., Boltyanskii, V. G., Gamkrelidze, R. V., & Mishchenko, E. F. (1962). *The mathematical theory of optimal processes*. Interscience Publishers.

[46]. Gelfand, I. M., & Fomin, S. V. (1963). *Calculus of variations*. Prentice-Hall.

[47]. Sobol, I. M. (2001). Global sensitivity indices for nonlinear mathematical models and their Monte Carlo estimates. *Mathematics and Computers in Simulation*, *55*(1–3), 271–280.

[48]. Saltelli, A., Annoni, P., Azzini, I., Campolongo, F., Ratto, M., & Tarantola, S. (2010). Variance based sensitivity analysis of model output. Design and estimator for the total sensitivity index. *Computer Physics Communications*, *181*(2), 259–270.

[49]. IPCC. (2021). *Climate change 2021: The physical science basis. Contribution of Working Group I to the Sixth Assessment Report of the Intergovernmental Panel on Climate Change*. Cambridge University Press.

انجمن مهندسی معدن ایران
نشریه مهندسی معدن و محیط زیست
نشانی نشریه: www.jme.shahroodut.ac.ir
دانشگاه صنعتی شاهرود

# بهینه‌سازی متغیرِ مسافت حمل باطله در معادن روباز مس-پورفیری عمیق تحت قید مرزی ژئومکانیکیِ متغیر با زمان

شیرزاد کریم‌اف* و الدور تویچی‌بویف

شعبه دانشگاه ملی علوم و فناوری «MISIS» در آلمالیق، جمهوری ازبکستان

**اطلاعات مقاله**

**تاریخ ارسال**: ۲۰۲۶/۰۶/۰۵
**تاریخ داوری**: ۲۰۲۶/۰۷/۲۷
**تاریخ پذیرش**: ۲۰۲۶/۰۹/۰۵

DOI: 10.22044/jme.2026.17793.3540

**کلمات کلیدی**

تخلیه مواد در نزدیکی دیواره
بهینه‌سازی مسافت حمل
پایداری شیب
کنترل بهینه
مسافت حمل مجاز از نظر ژئومکانیکی

**چکیده**

تخلیه باطله‌ها در نزدیکی دیواره‌های معادن روباز عمیق، مسافت حمل مواد باطله را کاهش می‌دهد؛ اما کوتاه‌ترین مسیر مجاز، تابع پایداری شیب دیواره است. در این پژوهش، مفهوم «مسافت حمل مجاز از نظر ژئومکانیکی» (GAHD) به عنوان یک کران پایینِ وابسته به زمان در مسئله بهینه‌سازی مسافت حمل (با در نظر گرفتن ارزش زمانی پول) تعریف و فرمول‌بندی شده است. چارچوب ارائه‌شده ترکیبی از روش‌های زیر است: تحلیل تعادل حدی دوبعدی، رابطه نیمه‌تجربی خطی (آفین) برای مصرف سوخت، مدل تجربی زمان چرخه، تعیین تعداد ناوگان حمل‌ونقل (به صورت اعداد صحیح)، حل مسیر حرکت با استفاده از روش تفاضل محدود (با رویکرد مجموعه فعال)، و تحلیل انتشار عدم‌قطعیت. نوآوری این پژوهش بیشتر جنبه روش‌شناختی و تلفیقی دارد تا ارائه یک الگوریتم جدید برای برنامه‌ریزی معدن. مطالعه موردی اصلی، معدن مس «کالماکیر» (متعلق به مجتمع معدنی و متالورژی آلمالیق در ازبکستان) است و بخشی از دیواره معدن «مورون‌تاو» نیز به عنوان نمونه‌ای دیگر برای بررسی مفهوم دپوی چندطبقه (چندترازه) مورد استفاده قرار گرفته است. در چهار دیواره معدن کالماکیر، مقدار GAHD بین ۱.۸۹۴ تا ۱.۹۶۵ کیلومتر متغیر است که میانگین وزنی آن (بر اساس میزان تولید) ۱.۹۰۹ کیلومتر محاسبه می‌شود. در مقایسه با یک سناریوی عملیاتی با مسافت حمل ۴.۵ کیلومتر، مدل نشان می‌دهد که در حالت مسافت ۲.۰ کیلومتر، مصرف سوخت از ۸۶.۰ به ۵۱.۲ لیتر در هر سرویس، زمان چرخه از ۳۶.۵ به ۳۱.۱ دقیقه، و تعداد ناوگان مورد نیاز از ۶۰ به ۵۱ دستگاه کامیون کاهش می‌یابد. از آنجا که مرز دیواره با سرعت تقریبی ۷.۲ متر در سال پیشروی می‌کند (شاخص جابه‌جایی مرز حدود ۰.۰۲ است)، استفاده از یک قید ثابت برای این بازه زمانی هفت‌ساله کفایت می‌کند؛ اما برای عملیاتی که در آن‌ها عمق معدن با سرعت بیشتری افزایش می‌یابد یا افق زمانی طولانی‌تری مد نظر است، باید از فرمول‌بندیِ مبتنی بر «مرز متحرک» استفاده کرد. تحلیل مونت‌کارلو با ۵۰,۰۰۰ تکرار، میانه «ارزش فعلی خالص» (NPV) را برابر با ۲۰.۰ میلیون دلار آمریکا نشان می‌دهد که بازه صدک پنجم تا نود و پنجم آن بین ۶.۷ تا ۳۴.۰ میلیون دلار است. تمامی پارامترهای کالیبره‌شده مختص این سایت معدنی هستند و پیش از به‌کارگیری در سایر معادن، نیازمند کالیبراسیون مجدد و اعتبارسنجی می‌باشند.

نویسنده مسئول مکاتبات: karimov20-13@mail.ru (ش. کریم‌اف)